PNAS RESEARCH ARTICLE | BIOCHEMISTRY OPEN ACCESS

Metal retention and replacement in QueD2 protect queuosine-tRNA biosynthesis in metal-starved *Acinetobacter baumannii*

Matthew R. Jordan[a,b], Giovanni Gonzalez-Gutierrez[b], Jonathan C. Trinidad[a,c], and David P. Giedroc[a,1]

Edited by Amy Rosenzweig, Northwestern University, Evanston, IL; received August 9, 2022; accepted October 28, 2022

In response to bacterial infection, the vertebrate host employs the metal-sequestering protein calprotectin (CP) to withhold essential transition metals, notably Zn(II), to inhibit bacterial growth. Previous studies of the impact of CP-imposed transition-metal starvation in *A. baumannii* identified two enzymes in the de novo biosynthesis pathway of queuosine-transfer ribonucleic acid (Q-tRNA) that become cellularly abundant, one of which is QueD2, a 6-carboxy-5,6,7,8-tetrahydropterin (6-CPH$_4$) synthase that catalyzes the initial, committed step of the pathway. Here, we show that CP strongly disrupts Q incorporation into tRNA. As such, we compare the *Ab*QueD2 "low-zinc" paralog with a housekeeping, obligatory Zn(II)-dependent enzyme QueD. The crystallographic structure of Zn(II)-bound *Ab*QueD2 reveals a distinct catalytic site coordination sphere and assembly state relative to QueD and possesses a dynamic loop, immediately adjacent to the catalytic site that coordinates a second Zn(II) in the structure. One of these loop-coordinating residues is an invariant Cys18, that protects QueD2 from dissociation of the catalytic Zn(II) while maintaining flux through the Q-tRNA biosynthesis pathway in cells. We propose a "metal retention" model where Cys18 introduces coordinative plasticity into the catalytic site which slows metal release, while also enhancing the metal promiscuity such that Fe(II) becomes an active cofactor. These studies reveal a complex, multipronged evolutionary adaptation to cellular Zn(II) limitation in a key Zn(II) metalloenzyme in an important human pathogen.

queuosine | QueD2 | tunnel-fold | zinc | nutritional immunity

Significance

A poorly understood aspect of the bacterial adaptive response to host-mediated Zn(II) restriction is the upregulation of functional paralogs to replace obligatory Zn(II)-dependent proteins. Here, we find that metal limitation disrupts the biosynthesis of queuosine-transfer RNA. We present the first structure of a "low zinc" paralog of 6-carboxy-5,6,7,8-tetrahydropterin (6-CPH$_4$) synthase, QueD2, and highlight key structural and metallocofactor-dependent differences relative to a housekeeping QueD. A key distinction is the presence of dynamic Zn(II) binding loop, incorporating an invariant cysteine, that slows dissociation of the catalytic metal of QueD2 in what is termed a "metal retention" model that is absent in QueD. This work highlights a mechanism in the adaptive response to Zn(II) limitation in an important human pathogen.

Metalloenzymes are predicted to constitute ≈30% of a typical bacterial proteome and are found in myriad metabolic pathways (1, 2). Cognate metal incorporation is required for proper enzymatic activity; mismetalation by a noncognate metal or undermetalation (substoichiometric metal occupancy) can result in severely attenuated or abolished turnover (3). In response to foreign bacterial pathogen invasion, neutrophils from the host are recruited to sites of infection where the major antimicrobial protein calprotectin (CP) is released to sequester Zn(II) and other essential transition metals [Fe(II), Mn(II), Ni(II), and Cu(II)], thereby inhibiting bacterial growth in an organism-specific fashion (4–10). This process of "nutritional immunity" is thought to result in undermetalation of metalloenzymes within the bacterial cell; however, the specific metabolic pathways that are disrupted under these conditions remain elusive (11–13). In liquid culture on a rich growth medium, CP withholds Zn(II) and Fe(II) from the major human pathogen *Acinetobacter baumannii* and attenuates bacterial growth in a mouse model of infection (7, 14). Under these conditions of multimetal starvation, two zinc metalloenzymes in the biosynthesis pathway of the tRNA modification queuosine (Q) become cellularly abundant, signifying either a failure or a prioritization of the pathway: QueD2, a putative 6-carboxy-5,6,7,8-tetrahydropterin (6-CPH$_4$) synthase, and tRNA-guanine transglycosylase Tgt, which inserts a Q precursor nucleobase into the mature tRNA in place of guanine (15–17).

tRNA modifications are ubiquitous and impact tRNA structure and function in the translation elongation cycle, affecting messenger ribonucleic acid (mRNA) decoding, ribosomal interactions, and amino-acylation (18). tRNA modifications, particularly in the tRNA anticodon loop, serve regulatory roles and impact both the speed and fidelity of protein translation by stabilizing selected codon–anticodon interactions (18, 19). Queuosine is a 7-deazaguanosine hypermodification found in the 34th (wobble) position of tRNAs within the $G_{34}U_{35}N_{36}$ (where A: adenosine; C: cytidine; G: guanosine; U: uridine; N; any nucleotide) anticodon where G_{34} is exchanged for the Q nucleotide (Fig. 1*A*) (20, 21). Although these four tRNAs, which decode Tyr, Asn, Asp, and His codons, recognize both synonymous NAC and NAU codons, the G-U mismatch in the wobble position destabilizes NAU codon–anticodon interactions (20, 22). The Q modification alleviates this decoding impairment by stabilizing base pairing with NAU codons, while possibly destabilizing interactions with NAC codons (20, 22–25), thereby enhancing

Author contributions: M.R.J. and D.P.G. designed research; M.R.J. and G.G.-G. performed research; J.C.T. contributed new reagents/analytic tools; M.R.J. and G.G.-G. analyzed data; and M.R.J. and D.P.G. wrote the paper.

The authors declare no competing interest.

This article is a PNAS Direct Submission.

[1]To whom correspondence may be addressed. Email: giedroc@indiana.edu.

This article contains supporting information online at https://www.pnas.org/lookup/suppl/doi:10.1073/pnas.2213630119/-/DCSupplemental.

Published November 29, 2022.

translation rates of NAU codons relative to that of NAC codons (Fig. 1*A*) (26, 27). Indeed, in the absence of the Q modification, ribosomes exhibit increased dwell times/stalling on NAU codons relative to NAC codons in eukaryotic cells (24). The Q modification also protects against near- and non-cognate codon misreading, primarily in the second position, and thus incorrect amino acid incorporation for certain codons (25, 28). Taken together, the Q incorporation enables rapid decoding of NAU codons while decreasing amino acid misincorporation, impacting both translational speed and fidelity; as a result, the loss of Q results in myriad, diverse physiological defects in eukaryotic systems (24, 25, 29–38). In contrast, the impact of Q-tRNA in bacteria is largely unexplored (38–40).

The global impact of the Q modification on protein translation rates likely varies among organisms, as the organismal requirement for Q may well be predetermined by the presence of NAU vs. NAC codons in the coding regions of the genome. Codon usage is reflected in the relative synonymous codon usage (RSCU) value, defined as the ratio of codons used in a gene or genome to the expected amount if all synonymous codons were used equally (41). For two synonymous codons, as is the case for all four Q-decoded codons, this value ranges from 0 to 2, with a value approaching two indicative of an overrepresentation of a particular codon relative to other synonymous codons. The *A. baumannii* genome is significantly enriched for all four NAU codons, in striking contrast to the *Escherichia coli* genome, for comparison (*SI Appendix*, Fig. S1 and Table 1). Moreover, all NAU codons in the *A. baumannii* genome must be decoded by a tRNA harboring the GUN anticodon loop and hence must overcome a wobble position mismatch, since *A. baumannii* does not encode a tRNA capable of making three Watson-Crick base pairs to any NAU codon. Thus, *A. baumannii*, like other organisms characterized by an overrepresentation of NAU codons, may well be more highly dependent on the Q modification for maintaining translation quality control and proteome maintenance.

The Q-tRNA biosynthesis pathway is remarkably complex with eight enzymatic steps, many of which require transition metals as cofactors. There are four Zn(II)-dependent enzymes (42–45), one radical SAM and 4Fe-4S cluster containing enzyme (46), and either one $(4Fe\text{-}4S)_2$ cluster and cobalamin-dependent enzyme (47) or one 4Fe-4S cluster containing enzyme (48) (Fig. 1*B*). Proper enzyme metalation is therefore required to sustain Q biosynthesis, and multimetal starvation may well impact flux through the pathway. Indeed the Q-tRNA biosynthesis pathway has been linked to Zn(II) starvation in a bioinformatics analysis in bacteria (49) and transcriptionally in higher-order eukaryotes (50), as well as exogenous exposure to other metals (40, 51–55).

The committed step of the Q-tRNA biosynthesis pathway (Fig. 1 *B* and *C*) is the conversion of 7,8-dihydroneopterin triphosphate (H_2NTP) to 6-carboxy-5,6,7,8-tetrahydropterin (6-CPH_4) by QueD or a QueD paralog, termed QueD2. Organisms encode either a QueD only, a QueD2 only (as in *A. baumannii*), or both a QueD and QueD2, with the latter often transcriptionally regulated by the zinc uptake repressor (Zur). QueD and the QueD2

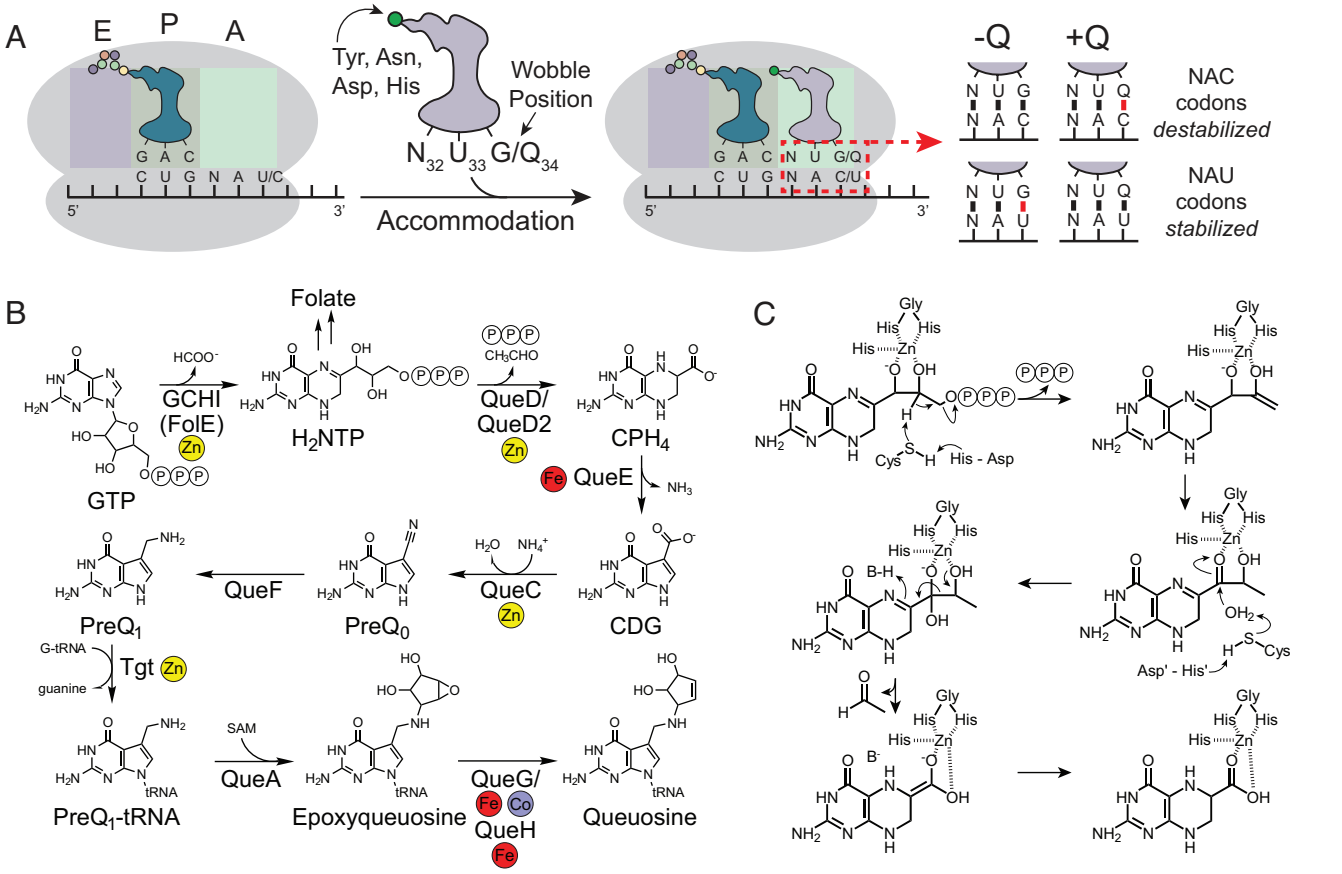

Fig. 1. Queuosine significance in *A. baumannii* and the QueD/QueD2 reaction mechanism. (*A*) Q modification occurs in the wobble position of a GUN anticodon-containing tRNA and functions in the accommodation step of protein translation by stabilizing interactions with NAU codons to enhance translation rate. (*B*) de novo Q-tRNA biosynthesis pathway with all metal-dependent enzymes highlighted. Zn(II), *yellow*-filled circle; Fe/Fe-S cluster, *red*-filled circle; and cobalamin, *slate*-filled circle. (*C*) Proposed catalytic mechanism of QueD/QueD2 converting H_2NTP to 6-CPH_4 (15). We note that the proton abstracted in the first step of the reaction could be either α- or β- to the imine functionality, with the β proton shown (15). The Cys nucleophile in both halves of the reaction is Cys23 in *Ab*QueD2.

Table 1. Codon usage table of common organisms and number of corresponding tRNA genes with triplet Watson-Crick base pairing to the indicated codon.

A. baumannii				*E. coli*	
Amino Acid	Codon	RSCU	tRNA genes	RSCU	tRNA genes
Asp	GAU	1.43	0	0.60	0
	GAC	0.57	3	1.40	3
His	CAU	1.48	0	0.45	0
	CAC	0.52	1	1.55	1
Asn	AAU	1.35	0	0.10	0
	AAC	0.65	4	1.90	4
Tyr	UAU	1.52	0	0.39	0
	UAC	0.48	1	1.61	3

paralog typically share less than 20% sequence identity, and a major distinguishing feature is that QueD2 incorporates a single amino acid insertion in the catalytic Cx_3HGH motif of QueD to create a Cx_4HGH motif in QueD2 (16). *E. coli* QueD is reported to be a Zn(II)-dependent enzyme, where the catalytic Zn(II) is coordinated by both His residues of the Cx_3HGH motif and a third more N-terminal His, which in turn coordinates the substrate and subsequent enzymatic intermediates in a pentacoordinate active site (15, 43). The catalytic Cys of the Cx_3HGH participates in two catalytic triads in the enzymatic reaction, the first of which is proposed to abstract a proton to allow for the elimination of triphosphate, while the second activates a water molecule for nucleophilic attack and subsequent acetaldehyde elimination (Fig. 1*C*) (15). Although complementation of an *E. coli* Δ*queD* strain with an *Ec*QueD catalytic variant (Cx_3HGH motif converted to Cx_4HGH) or *Acinetobacter baylii* QueD2 each recover Q incorporation onto mature tRNA (16), the QueD2 paralog has not yet been structurally and biochemically characterized.

Here, we show that exogenous CP directly inhibits Q-tRNA biosynthesis in *A. baumannii*, which modestly impacts bacterial growth. We identify the key primary structure and genomic location determinants that distinguish a QueD from a QueD2. We present the first structure of any QueD2, from *A. baumannii*, and biochemically characterize metal binding and metal-dependent enzymatic activity of the enzyme. Moreover, we identify a set of QueD2-specific Zn(II)-binding residues that define a second site of lower affinity, not present in QueD, that we propose introduces coordinative plasticity into the catalytic metal site. Conserved Cys18 of this second metal site renders QueD2 less susceptible to Zn(II) dissociation of, and flux through, the Q biosynthesis pathway in *A. baumannii*, yet paradoxically, when filled, inhibits turnover. We propose a "metal retention" model that allows QueD2 to function under conditions of low bioavailable Zn(II) that cannot be accomplished by overexpression of the enzyme alone.

Results

CP Inhibits Queuosine-tRNA Biosynthesis. In an effort to link the increase in protein abundance of the Q biosynthetic enzymes QueD2 and Tgt in response to CP-induced multimetal starvation (7), we quantified the amount of Q modification in mature tRNA from *A. baumannii*. Bulk tRNA was extracted from wild-type (WT) and Δ*queD2* cells grown on *U*-^{12}C-acetate as the sole carbon source in the presence and absence of various physiological concentrations of exogenous CP and mixed 1:1 (mol nucleotide)

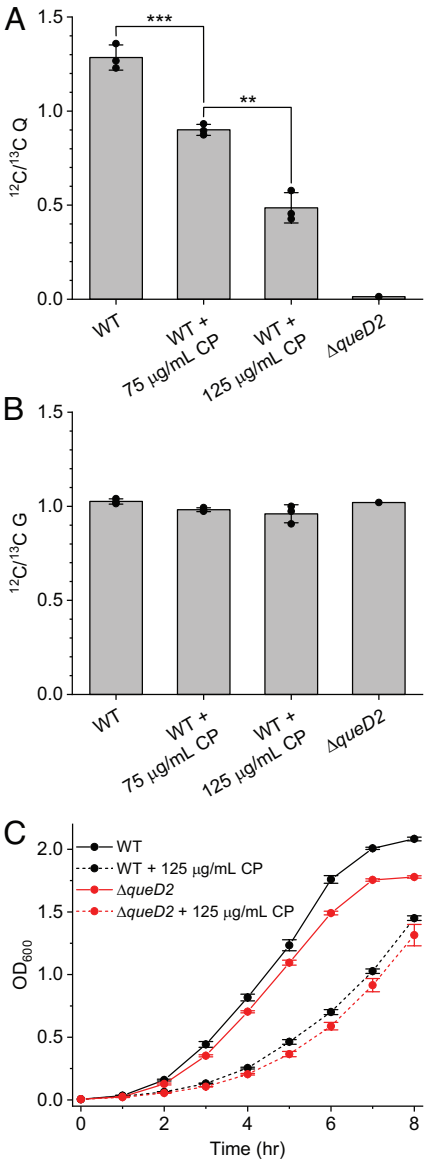

Fig. 2. Q-tRNA biosynthesis in *A. baumannii* physiology. Total queuosine (Q, panel *A*) and guanosine (G, panel *B*) levels in tRNA isolated from *A. baumannii* under unstressed conditions and increasing amounts of CP, with the null (Δ*queD2* strain) condition. (*C*) Growth of WT and Δ*queD2 A. baumannii* cells in chemically defined HHWm with or without exogenous CP. Data are shown as average ± SD for each panel. For panel *A*, data were analyzed by Student's *t* test using Welch's correction, ** indicates $P < 0.01$, *** indicates $P < 0.001$.

with a tRNA preparation extracted from WT cells grown on *U*-^{13}C-acetate. The latter is used as an internal "spike" for this isotope dilution mass spectrometry experiment (*SI Appendix*, Fig. S2*A*). This tRNA mixture was digested into nucleosides and analyzed by liquid chromatography-mass spectrometry (LC–MS) and ratiometric quantification of the $^{12}C/^{13}C$ Q base peak intensities measured (*SI Appendix*, Fig. S2 *B–D*). These data reveal decreased total Q levels in the tRNA pool in response to increasing amounts of CP-mediated metal starvation revealing that CP inhibits Q-tRNA biosynthesis (Fig. 2*A*). Under the same conditions, there is no impact on the recoveries of any other unmodified tRNA nucleoside as a function of CP or in the Δ*queD2* strain, suggesting that the trend that we see with Q is highly specific (Fig. 2*B* and *SI Appendix*, Fig. S2*E*). The Δ*queD2* strain grows more slowly than WT and reaches a lower growth yield, and this growth defect remains in the Δ*queD2* strain in the presence of exogenous CP (Fig. 2*C*).

Defining QueD and QueD2 Characteristics. In order to examine CP-mediated inhibition of the Q biosynthesis pathway, we chose to evaluate QueD2 as the potential bottleneck, as it catalyzes the committed step in the pathway, becomes cellularly abundant under multimetal restriction (7), and is entirely uncharacterized. Moreover, *A. baumannii* does not encode a QueD but only a QueD2 paralog that is not Zur-regulated but becomes cell abundant via an as yet undefined posttranscriptional mechanism under low-zinc conditions. Both QueD and QueD2 belong to the 6-pyruvoyl-tetrahydopterin synthases (PTPS) superfamily (Pfam PF01242), which also harbors enzymes that instead direct H_2NTP into tetrahydrofolate, biopterin, or archaeosine biosynthesis (16). Of the six identifiable PTPS classes as defined by their catalytic motifs, PTPS-I includes 6-carboxy-5,6,7,8-tetrahydropterin synthases QueD and QueD2 involved in the tRNA modifications Q and archaeosine, PTPS-II enzymes form 6-pyruvoyltetrahydropterin in biopterin biosynthesis, and PTPS-III enzymes synthesize H_2-pterin-CH_2OH for folate metabolism (16).

Using genomic enzymology tools (56), 34, 387 total PTPS sequences were segregated into a sequence similarity network (SSN) containing 111 distinct clusters (*SI Appendix*, Fig. S3). Individual SSN clusters were assigned to PTPS subfamilies based on conserved catalytic motifs identified from a multiple sequence alignment. QueD (55%) and QueD2 (9%) proteins make up the vast majority of the PTPS family members (64% of the total), while PTPS-II enzymes are the next largest group of enzymes (at 21%); the remaining PTPS subgroups were minimal (<2%) or unidentifiable (14%) in this analysis (*SI Appendix*, Fig. S4 *A* and *B*). On the basis of the conserved Cx_3HGH catalytic motif, 61 clusters were classified as QueD proteins (*SI Appendix*, Figs. S4 *C–G* and S5) (15).

QueD2s were readily identified in SSN clusters 5 and 10 (Fig. 3; SSN clusters ranked according to number of sequences). *Ab*QueD2 is contained within SSN cluster 5, which is 190 to 200 amino acids in length, and includes a C-terminal extension relative to QueDs (Fig. 3*A* and *SI Appendix*, Fig. S4*H*). Cluster 5 QueD2s contain high similarity across the N-terminal domain, notably containing the Cx_4HGH motif, the predicted third Zn(II)-coordinating His, the anticipated catalytic triad residues, and an invariant Cys residue (Cys18 in *Ab*QueD2) located between the catalytic Cys and the predicted third His metal ligand (*SI Appendix*, Fig. S6*A*). In contrast, cluster 10 QueD2s are 275 to 300 amino acids in length, with an additional N-terminal domain of ≈180 residues of unknown function (Fig. 3*B* and *SI Appendix*, Fig. S3*I*). The C-terminal domain of cluster 10 QueD2s possesses the core catalytic Cx_4HGH residues, the predicted third Zn(II)-coordinating His, and an invariant His residue located between Zn(II)-coordinating residues and the catalytic Cys, in a position that is similar to that of Cys18 in *Ab*QueD2 (*SI Appendix*, Fig. S6*B*).

An analysis of the genomic localization of *queD2*, shown as representative genomic maps for cluster 5 and 10 proteins (Fig. 3 *C* and *D*), reveals that both clusters harbor *queD2* genes that are predicted to be regulated by Zur and thus are only expressed under low cellular Zn(II); however, these represent only a fraction of all QueD2-encoding genes and cannot be differentiated from non-Zur-regulated *queD2* at the primary structure level. The *queD2* of *Burkholderia cepacia, Cupriavidus metallidurans*, and *Klebsiella pneumoniae* (this *queD2* is truncated) colocalize with genes encoding other enzyme paralogs and putative COG0523-family Zn(II) metallochaperones, known members of Zur regulons (49, 57, 58). These three organisms encode a *queD* found elsewhere in the genome, suggesting that the maintenance of Q biosynthesis, specifically under low Zn(II), is important for the growth of these organisms under conditions of Zn(II) starvation. For the remaining *queD2* genes not predicted to be part of a Zur regulon, there is some genomic association with *folE* and *queE*, the genes encoding proteins preceding and following QueD2 in the de novo Q-tRNA biosynthesis pathway. Additionally, there is some colocalization with a gene encoding a GTP 3,8-cyclase which functions in the molybdopterin biosynthesis pathway, initiated by PTPS-III enzymes (16). In these organisms, like in *A. baumannii*, QueD2 is the only genomically encoded 6-CPH_4 synthase and is either expressed in a way that is independent of cellular Zn(II) concentration or is regulated in some other way, e.g., post-transcriptionally, by zinc availability.

QueD2 Structure. We next solved the crystallographic structure of *A. baumannii* QueD2 bound to Zn(II) to 2.35 Å resolution (*SI Appendix*, Table S1). The asymmetric unit includes two QueD2 molecules and four Zn(II) ions, and generation of symmetry mates yields the octameric assembly state, which is also observed in solution (Fig. 4*A* and *SI Appendix*, Fig. S7*A*). QueD2, like *E. coli* QueD (15), is a member of the tunnel-fold (T-fold) superfamily despite low sequence similarity (Fig. 4*B*) (59). T-fold protein protomers are characterized by a ββααββ topology (Fig. 4*C*) that assemble into two oligomeric ring structures stacked head-to-head. The center of the T-fold "tunnel" is lined with antiparallel β-strands with the α-helical bundles on the periphery. Although the stacked ring structure in T-fold proteins is conserved, there is a vast diversity of assembly states, ranging from two dimeric rings (60) to two pentameric rings (61). QueD2 consists of two tetrameric rings stacked head-to-head in the octameric assembly with each protomer contributing all four β-strands (β1–β4; Fig. 4*C*) to create a 16-stranded, antiparallel β-barrel "tunnel" (Fig. 4*A*). This assembly state is notably distinct from that of QueD, which adopts two stacked trimeric rings and thus a 12-stranded, antiparallel β-barrel (Fig. 4*B*). Outside of the core ββααββ topology, both QueD2 and QueD possess a small insertion between α1 and α2 (Fig. 4*C*); the longer QueD2 insertion contains two parallel β-strands and an α-helix, while the shorter QueD insertion features a β-meander and a short α-helix (Fig. 4 *C–E*). QueD2 additionally contains a C-terminal extension following β4 which consists of short α-helices and random coil motifs that are packed on the periphery of the oligomeric ring (Fig. 4 *C* and *D*). Although *Ec*QueD and *Ab*QueD2 adopt distinct oligomeric states, the structure of the core ββααββ architecture aligns with striking similarity (2.91 Å root-mean-square deviation [RMSD], *SI Appendix*, Fig. S7 *B–D*). The interaction between subunits within each ring is defined by interactions between the β1 and β4′ of adjacent subunits, with the intertetramer interaction composed of hydrophobic packing and the catalytic Zn(II) site (site 1, see below).

There are two distinct Zn(II) binding sites in the *Ab*QueD2 structure compared to the single crystallographically captured Zn(II) binding site in *Ec*QueD. The active site, Zn1, is coordinated by two residues from one protomer (H28, H30 from the Cx_4HGH motif) and one residue from the opposite protomer (H68", Fig. 4*F*). This site exhibits trigonal bipyramidal Zn(II) coordination by His28, His30, His68" (intertetrameric bridging), and two water molecules (Fig. 4*F* and *SI Appendix*, Fig. S7 *E* and *F*) that are likely displaced by substrate and enzymatic intermediates, as in the *Ec*QueD structure (Fig. 4*G*) (15). Surprisingly, the *Ab*QueD2 site 1 coordination sphere is spatially shifted relative to that of ligand-bound *Ec*QueD. Zn(II) coordination by the two His residues of the HGH motif is conserved in both enzymes; however, His13 in *Ab*QueD2 (analogous to His16 in *Ec*QueD)

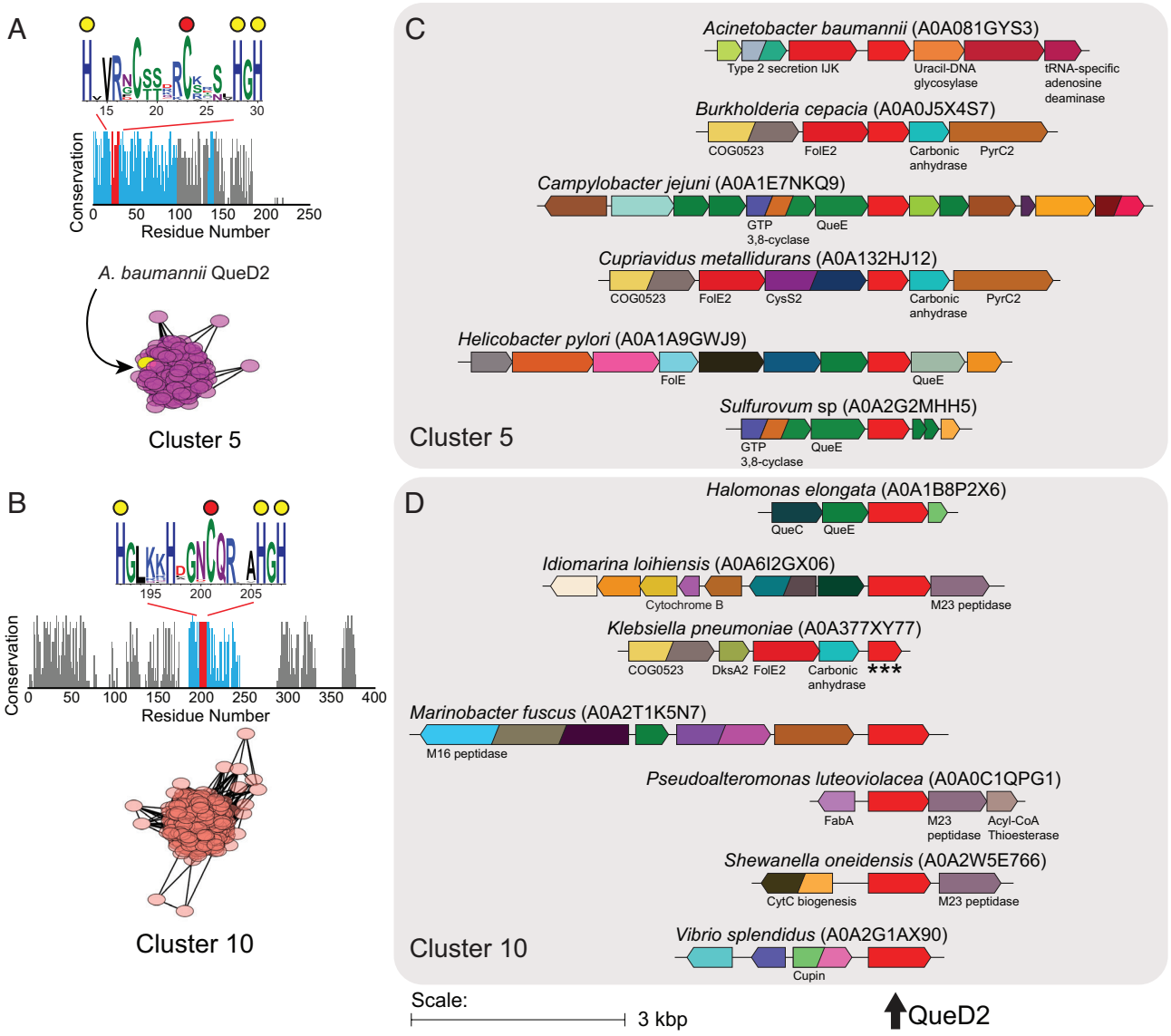

Fig. 3. SSN and GNN analysis of QueD2 proteins. Sequence conservation and cluster of (*A*) cluster 5 and (*B*) cluster 10 QueD2 proteins with a logo plot of the conserved catalytic region (*Top*). This conserved catalytic region is highlighted in *red* in the conservation plot and QueD-like regions are labeled in *blue*. Predicted metal binding residues are indicated with *yellow* spheres, and the predicted catalytic Cys residue is indicated with *red* spheres. *A. baumannii* QueD2 is highlighted yellow and indicated within cluster 5. Representative genomic neighborhoods of (*C*) cluster 5 and (*D*) cluster 10 QueD2 proteins from select organisms. *** indicates a truncated *queD2* gene.

does not coordinate to Zn(II) and instead His 68", analogous to His71" in *Ec*QueD and in the first catalytic triad required for enzymatic turnover (15) (Fig. 1*C*), does. This hints at a coordinative heterogeneity in the catalytic site of *Ab*QueD2 that is not present in the ligand-free structure of *Ec*QueD (15). The second site, Zn2, includes two coordinating residues (invariant C18 and C23 in the $\underline{C}x_4$HGH motif) derived from one protomer and two other coordinating residues (H45′ and H188′) derived from the adjacent subunit within a tetramer (Fig. 4*H*) in a distorted tetrahedral coordination geometry. Notably, Cys18 is invariant in cluster 5 QueD2s (Fig. 3*A*), while cluster 10 QueD2s feature a conserved His in this position (Fig. 3*B*); this suggests that metal coordination here is conserved in all QueD2s. Cys23 is also conserved but represents the catalytic Cys in the $\underline{C}x_4$HGH motif that is required for enzymatic activity (see below).

Zn1 and Zn2 are in close proximity (separated by ≈14 Å) at the interface between subunits. The active site region and the catalytic Zn1 bridges the tetrameric rings, while Zn2 is interprotomer and very close to the protein surface (Fig. 4*I*). Moreover, the loop comprising Cys18 and Cys23 that coordinates Zn2 may well be highly mobile; this loop has relatively high B-factors in one monomer of the asymmetric unit and cannot be resolved in the second monomer despite the presence of anomalous Zn(II) density (*SI Appendix*, Fig. S7*G*). We also note that the one-residue insertion in the $\underline{C}x_4$HGH motif in QueD2 displaces the active site nucleophile (Cys23) by ≈3 Å relative to Cys27 of the $\underline{C}x_3$HGH motif in *Ec*QueD, which results from an unwinding of a short α-helix that places Cys27 very close to the active site metal in *Ec*QueD (*SI Appendix*, Fig. S7*H*). These data suggest that Cys18, Cys23, and the Zn2 loop in *Ab*QueD2 exhibit significant motional disorder even when bound to metal, a structural feature that distinguishes QueD2 from QueD (15).

QueD2 Metal Binding Properties. We next defined the affinities of two Zn(II) sites from the *Ab*QueD2 structure using metal binding competition experiments in solution. Titrations against quin-2 (K_{Zn} = 2.0×10^{11} M^{-1}, fluorescence is quenched upon Zn[II] binding) reveal that *Ab*QueD2 binds Zn(II) to form one high-affinity site

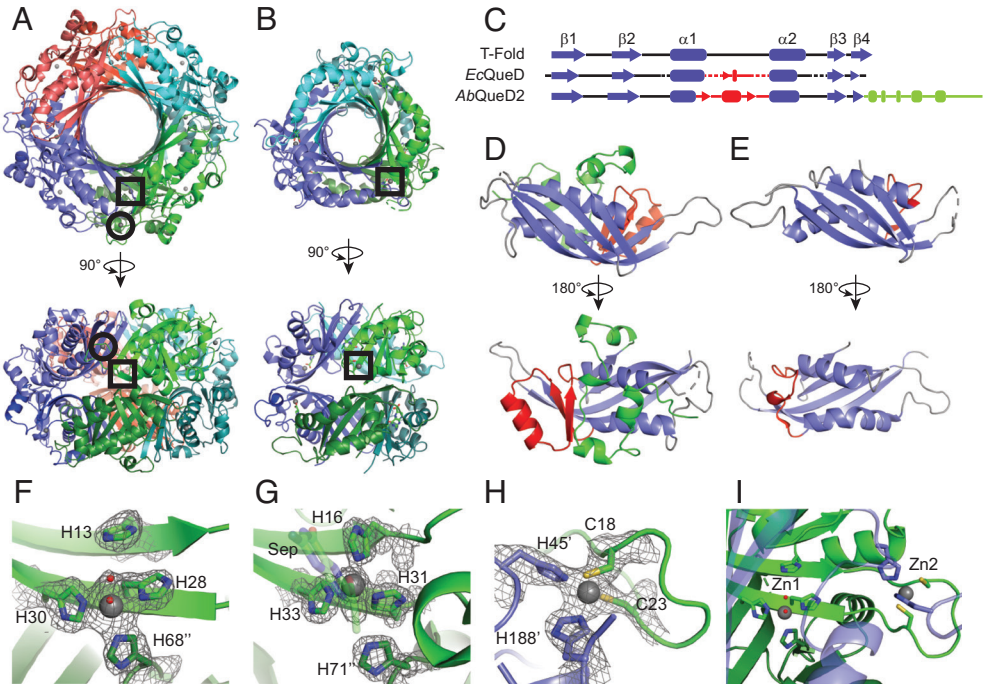

Fig. 4. *A. baumannii* QueD2 structure. Cartoon representation of (*A*) the octameric structure of T-fold member *A. baumannii* QueD2 and (*B*) the hexameric structure of *E. coli* QueD (PDB: 4 ntm) with top and side views. Individual monomers within the assembly are differentially colored, Zn(II) atoms are represented as gray spheres, the catalytic Zn1 site is located within a black square, and the unique QueD2 Zn2 site is located within a black circle. (*C*) Secondary structure alignment of conserved T-fold architecture (*Top*), *E. coli* QueD (*Middle*), and *A. baumannii* QueD2 (*Bottom*). α helices are depicted as rounded boxes, β strands are depicted as arrows, the core ββααββ topology is shown in blue, insertions observed in QueD/QueD2 proteins are shown in red, the QueD2 C-terminal extension is shown in green, and regions from QueD2 that are lacking in QueD are shown with dashed lines. (*D*) *A. baumannii* QueD2 and *E*) *E. coli* QueD (PDB: 4 ntm) monomer as viewed from within the tunnel (*Top*) and outside of the tunnel (*Bottom*) with structural regions labeled and colored as in panel *C*. Shifted coordination spheres of the catalytic Zn1 site of (*F*) *A. baumannii* QueD2 and (*G*) *E. coli* QueD (PDB: 4 ntk) bound to sepiapterin (Sep, transparent sticks). (*H*) Zn2 site that is unique in *A. baumannii* QueD2. (*I*) Zn1 and Zn2 are located near to one another, separated by ≈14 Å. For panels *F–I*, conserved residues are shown as sticks and labeled, Zn(II) atoms are represented as gray spheres, water molecules are represented as red spheres, and, for panels *F–H*, electron density is shown as gray mesh with $2F_o$-F_c electron density maps contoured at 1.5 σ.

(K_{Zn1}= 1.0±0.1×10^{11} M^{-1}, Fig. 5*A* and *SI Appendix*, Table S2). Mag-fura-2 (mf2, K_{Zn} = 5.0×10^{7} M^{-1}) was used to show that *Ab*QueD2 also possesses one low affinity Zn(II) site (K_{Zn2} = 4.7±0.2×10^{7} M^{-1}, Fig. 5*B* and *SI Appendix*, Table S2). We assigned the high-affinity site as anchored by the conserved catalytic HGH motif Zn1 site and the lower affinity, highly dynamic site to the Cys_2His_2 Zn2 site. We note, however, that this low affinity of the Zn2 site suggests that it will not be occupied by Zn(II) in the cell (62) and thus must play some other role (see below).

As other paralogous enzymes have been proposed to utilize alternative metals to Zn(II), we next assessed the QueD2 Fe(II) binding affinity by titration against mf2 ($K_{Fe(II)}$ = 2.8×10^{5} M^{-1}). We find that QueD2 binds one mol equivalent of Fe(II) with a $K_{Fe(II)}$ value of 1.3±0.1×10^{5} M^{-1} (Fig. 5*C* and *SI Appendix*, Table S2). Next, we performed Co(II) binding titrations to apo-QueD2 in an effort to assess the nature of the first coordination shell as QueD2 is titrated with Co(II) (63) (Fig. 5*D*). Contrary to the anticipated ordered filling of site 1 (containing no Cys) followed by site 2 (with two Cys), given their relative Zn(II) affinities (*SI Appendix*, Table S2), a prominent Cys-S^{γ}-to-Co(II) ligand to metal charge transfer (LMCT) absorption band in the near ultraviolet is clearly present as the first equivalent of Co(II) is added. At stoichiometric Co(II), this intense near-UV band is accompanied by weak absorption at 535 nm (ε ≈ 160 M^{-1} cm^{-1}) and *d-d* absorption bands observable at 630 nm and 670 nm with ε ≈ 500 M^{-1} cm^{-1} and 350 M^{-1} cm^{-1}, to create absorption spectrum that is broadly consistent with a single Cys-containing distorted tetrahedral complex. At 2 mol equivalents, each of these features grows slightly more prominent. These data suggest nonnative Cys recruitment into the high-affinity site 1, distinct from the crystallographic site 1, with saturated spectra consistent with the formation of both five- and four-coordinate complexes during the course of the titration.

Evaluating the Functional Significance of Site 2. To evaluate the role of the unique QueD2 Zn(II) site 2 residues, we substituted the conserved Cys18 to Ser (C18S). This mutation decreases site 2 Zn(II) binding affinity by ≈three-fold (K_{Zn2}=1.4±0.1×10^{7} M^{-1}) and also decreases catalytic site 1 Zn(II) binding affinity by ≈three-fold (K_{Zn1}=2.9±0.1×10^{10} M^{-1}, *SI Appendix*, Fig. S8 *A* and *B* and Table S2). This suggests that there is a physical connection between each crystallographic metal site, mediated by Cys18, potentially consistent with the Co(II)-titration experiments. We next elucidated the in vivo function of Cys18 by complementing the Δ*queD2* strain with WT (Δ*queD2*::*queD2*) and site 2 residue mutant (Δ*queD2*::*queD2 C18S*) QueD2 expressed from a constitutive promoter on an extrachromosomal plasmid and measuring total Q-tRNA content. In the absence of CP, both Δ*queD2*::*queD2* and Δ*queD2*::*queD2 C18S* exhibit an increase in Q-tRNA content relative to that found in WT *A. baumannii*, which can be traced in part to a ≈150-fold increase in cellular QueD2 that is unchanged by extracellular CP (Fig. 6*A* and *SI Appendix*, Fig. S8*C*). Strikingly, overexpression of WT QueD2 is completely resistant to CP-mediated disruption of Q biosynthesis, while C18S QueD2 fails to maintain Q-tRNA levels to the same degree (Fig. 6*A*). The same is true following complementation and overexpression of *Staphylococcus aureus* QueD (Δ*queD2*::*queD*), which also lacks site 2 metal binding residues (Fig. 6*A*). As a control, Cys23 is

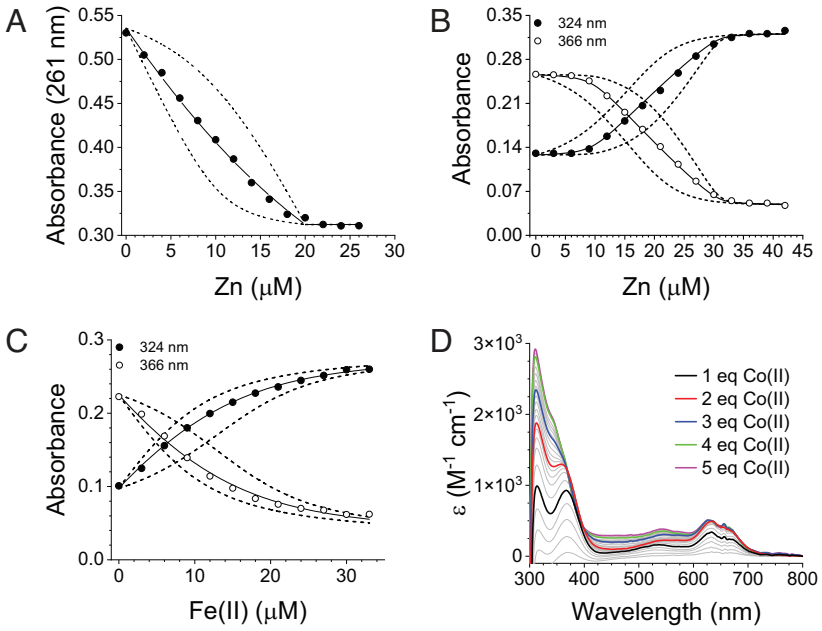

Fig. 5. QueD2 metal binding. (*A*) Representative titration of 10 μM QueD2 and 10 μM quin-2 with Zn(II). (*B*) Representative titration of 10 μM QueD2 and 10 μM mag-fura-2 with Zn(II). (*C*) Representative titration of 10 μM QueD2 and 10 μM mag-fura-2 with Fe(II). For panels *A*–*C*, all fitted affinity constants are compiled in *SI Appendix*, Table S2, solid lines represent a global fit from three replicate experiments of varying protein and chelator concentrations, and dashed lines represent simulated fits of ten times greater and weaker affinities at each binding site. (*D*) UV–Vis spectra of 250 μM QueD2 at increasing molar equivalents of Co(II) as indicated in the *Inset*.

absolutely required for turnover since complementation with Δ*queD2*::*queD2 C23A* abrogates Q-tRNA biosynthesis (Fig. 6*A*), as in the Δ*queD2* strain (Fig. 2*A*). These findings suggest that WT QueD2, via Cys18, makes QueD2 more resistant to CP-mediated metal restriction beyond that which could be accomplished by cellular overexpression alone.

To further understand the impact on site 1 Zn(II) binding by the site 2 C18S mutation, the kinetics of Zn(II) binding at site 1 specifically were evaluated using the high-affinity fluorescent Zn(II) chelator quin-2 (K_{Zn}=2×10^{11} M^{-1}, fluorescence is quenched upon Zn(II) binding). To estimate the on-rate of Zn(II) binding, quin-2 was preloaded with 0.75 mol equivalents of Zn(II), followed by the addition of excess apo QueD2. This results in a return of quin-2 fluorescence over time as Zn(II) binds specifically at the catalytic site of QueD2, which is optically transparent in this assay (*SI Appendix*, Fig. S8*D*). The resultant kinetic data are well-fitted to a single exponential function, from which the apparent pseudo-first-order association rate, k_{on} of Zn(II) binding at site 1, can be determined (*SI Appendix*, Fig. S8*D*). The C18S substitution has a modest increase in the rate at which Zn(II) binds to the enzyme relative to WT QueD2 (Fig. 6*B* and *SI Appendix*, Fig. S8*F*); thus, differences in the on-rate are unlikely to account for the lower equilibrium affinity of site 1 in C18S QueD2. Next, Zn(II) dissociation rates were estimated by preloading QueD2 with 0.75 mol equivalents of Zn(II) bound specifically to the conserved catalytic site 1 and adding this mixture to apo quin-2,

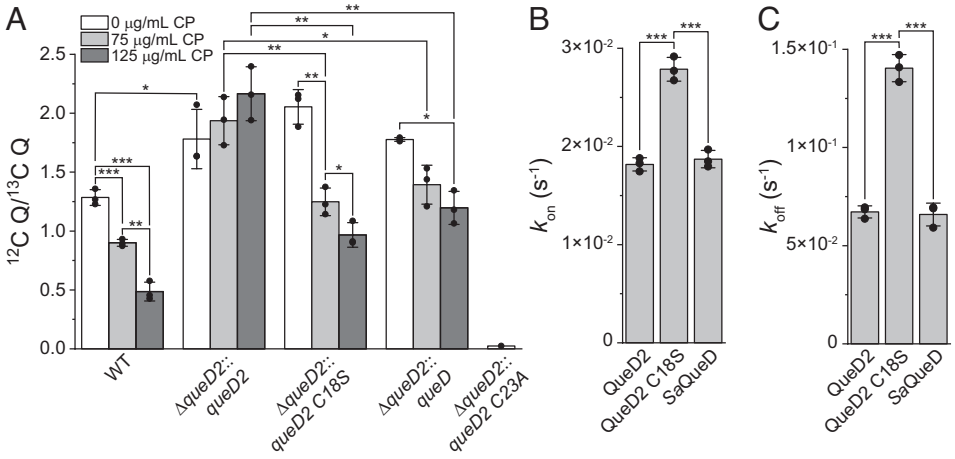

Fig. 6. QueD2 site 2 kinetically enables resistance to undermetalation. (*A*) Total Q in mature tRNA isolated from WT *A. baumannii* cells (reproduced from Fig. 2*A* for comparison) or Δ*queD2* complemented strains expressing only QueD2 (Δ*queD2*::*queD2*), QueD2 site 2 mutant (Δ*queD2*::*queD2 C18S*), *S. aureus* QueD (Δ*queD2*::*queD*), or QueD2 catalytic C23A mutant (Δ*queD2*::*queD2 C23A*) treated with 0, 75, or 125 μg/mL CP. The apparent on (*B*) and off (*C*) rate of Zn(II) binding by QueD2, QueD2 C18S, and *S. aureus* QueD. Data are shown as average ± SD and were analyzed by Student's *t* test using Welch's correction, * indicates $P < 0.05$, ** indicates $P < 0.01$, *** indicates $P < 0.001$.

where quin-2 fluorescence decreases as Zn(II) dissociates from the enzyme and binds quin-2 (*SI Appendix*, Fig. S8*E*). We find that C18S QueD2 exhibits a two-fold *increase* in the rate of site 1 dissociation rate compared to WT QueD2. These data provide support for a model in which site 2 residues, particularly Cys18, slow the release of Zn(II) from catalytic site 1 (Fig. 6*C* and *SI Appendix*, Fig. S8*G*). *Sa*QueD binds Zn(II) at the catalytic site 1 with an equilibrium affinity and Zn(II) binding kinetics that are indistinguishable from that of WT QueD2 (Fig. 6 *B* and *C* and *SI Appendix*, Fig. S8 *H–K* and Table S2). These data taken collectively suggest that the distinct functional properties of *Ab*QueD2 become apparent only under conditions of extreme metal depletion and confer resistance to CP-mediated disruption of Q-tRNA production mediated by site 2 Zn(II) binding residues or the invariant Cys18, specifically. This "metal retention" model allows *Ab*QueD2 to retain significantly more catalytic metal ion as bioavailable [Zn(II)] falls in the cell.

QueD2 and QueD Exhibit Similar Catalytic Metal Site Promiscuities but Distinct Activities. We next sought to evaluate the metal dependence of the enzymatic activity of QueD2 relative to QueD using an anaerobic, absorbance-based assay as substrate H_2NTP and product 6-CPH$_4$ have different spectroscopic characteristics (15). As predicted by prior studies of *Ec*QueD (15), we observe the formation and decay of a sepiapterin (Sep)-like intermediate (λ_{max} ≈ 400 nm) and therefore utilize a two-step kinetic model (Fig. 7*A*). Here, k_1 is the rate of triphosphate elimination to form the Sep-like intermediate and k_2 is the rate of acetaldehyde elimination to form the 6-CPH$_4$ product (15) (see Fig. 1*C*). We also observe the slow oxidation of 6-CPH$_4$ to 6-carboxypterin (6-CP), presumably due to trace amounts of oxygen, and include this in the kinetic model as k_{ox} (Fig. 7*A*). Full absorbance spectra collected over time were deconvoluted according to this three-step sequential model using single-value decomposition (SVD) to yield the molar absorptivity spectra of the substrate, intermediate, and products, as well as their rates of appearance and disappearance over time (Fig. 7*B* and *SI Appendix*, Fig. S9 *A* and *B*).

QueD2 exhibits slow 6-CPH$_4$-ase activity as confirmed by LC–MS/MS (Fig. 7*C* and *SI Appendix*, Fig. S9 *C* and *D*) in the presence of stoichiometric Zn(II). Since the catalytic Cys23 is coordinated to Zn(II) site 2 in our structure, we next evaluated the activity of QueD2 in the presence of two molar equivalents of Zn(II) and found that both steps of the enzymatic reaction are indeed inhibited as expected. We then measured *Sa*QueD enzymatic activity in the presence of Zn(II) to identify any functional distinctions between QueD and QueD2 enzymes (Fig. 7 *C* and *D*). *Sa*QueD exhibits a 10-fold increase in k_1 and a slight increase in k_2 relative to WT QueD2 with stoichiometric Zn(II) and is only modestly inhibited by excess Zn(II) (Fig. 7 *C* and *D*). Surprisingly, C18S QueD2 possesses *Sa*QueD-like Zn(II)-dependent kinetic characteristics and similarly is only modestly inhibited by excess Zn(II) (Fig. 7 *C* and *D*). This reveals that loss of Cys18 in site 2 reverts QueD2 Zn(II)-dependent activity to that of QueD-like enzyme.

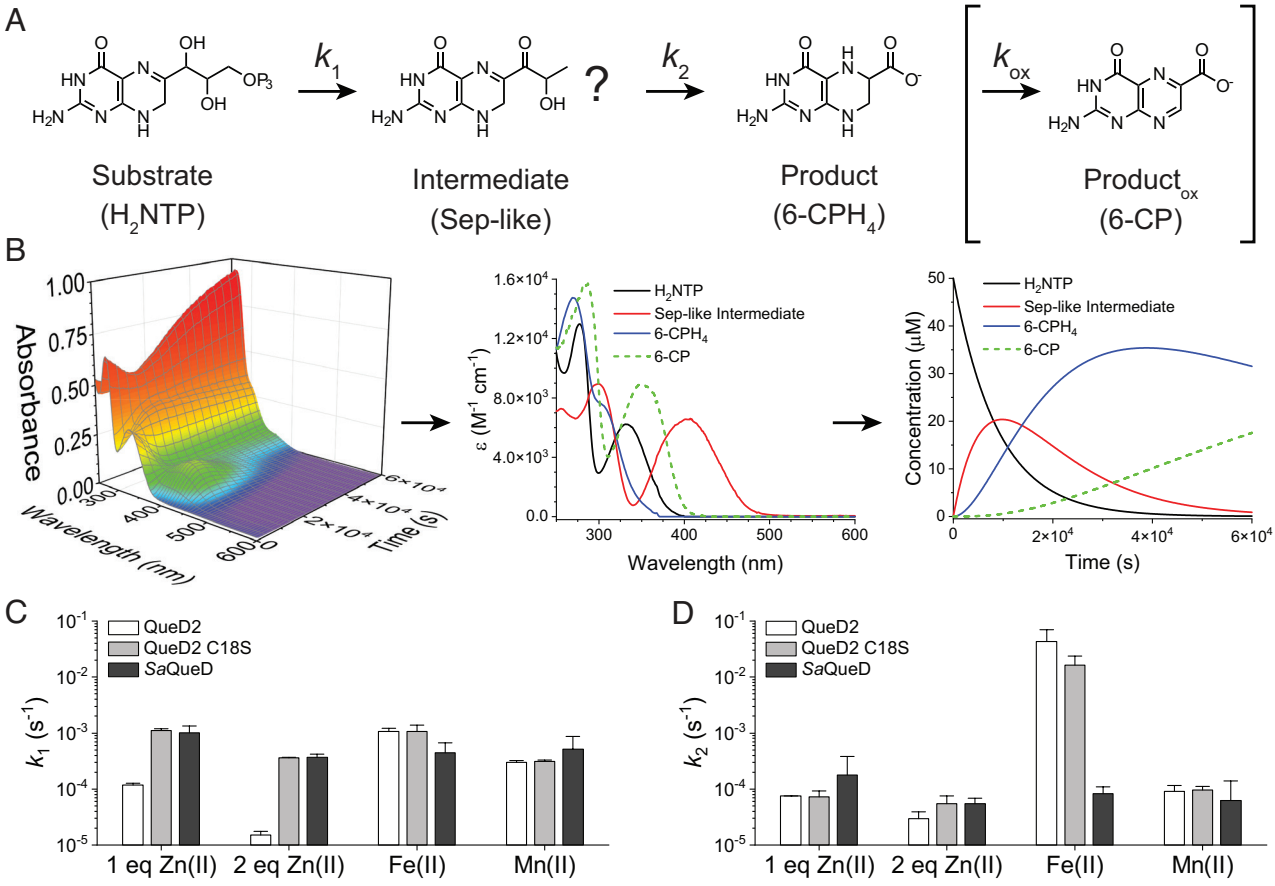

Fig. 7. 6-CPH$_4$ synthase activity. (*A*) Kinetic model utilized in this analysis based upon the proposed QueD/QueD2 mechanism (15) and the observable spectroscopic features. (*B*) Representative absorbance spectra of QueD2 enzymatic activity in the presence of 1 molar equivalent of Zn(II) as a function of time (*Left*). Spectra are deconvoluted using SVD to yield spectra of individual components (*Middle*) and the concentration of each component as a function of time (*Right*), as established by the kinetic model in panel *A*. (*C*) k_1 and D) k_2 values of 2 μM QueD2, QueD2 C18S, and *Sa*QueD in the presence of 2 μM Zn(II), 4 μM Zn(II), 2 μM Fe(II), and 10 μM Mn(II) as fit to the kinetic model in panel *A*. Data in panels *C* and *D* are from duplicate reactions and shown as average ± SD.

Due to the proposed metal promiscuity of other Zur-regulated protein paralogs (60), we evaluated the Fe(II)- and Mn(II)-dependent enzymatic activities of WT QueD2, C18S QueD2, and *Sa*QueD. We find that *Sa*QueD is active with both Fe(II) and Mn(II), although to perhaps a lesser extent than with the cognate metal Zn(II). WT QueD2 exhibits significant activity in the presence of Mn(II), comparable to that of Zn(II), but unlike QueD, is strongly activated by Fe(II), particularly in k_2 where the Sep-like intermediate is essentially unobservable (Fig. 7 *C* and *D* and *SI Appendix*, Fig. S9*E*). While the QueD2 C18S Zn(II)-dependent activity is like that of *Sa*QueD, it retains the WT QueD2-like Fe(II)-dependent activity (Fig. 7*C*), with k_2 slightly slower, consistent with more observable Sep-like intermediate in the absorbance spectra (*SI Appendix*, Fig. S9*F*). Notably, QueD2 C18S and *Sa*QueD bind Fe(II) with nearly indistinguishable affinities relative to WT QueD2 (*SI Appendix*, Fig. S9 *G* and *H* and Table S2). We conclude that both QueD and QueD2 are somewhat more metal promiscuous than previously reported but that Fe(II) is 100-fold more active in a QueD2 relative to QueD, in a way that appears largely independent of the presence of Cys18.

Discussion

Here, we show that the Q-tRNA biosynthesis pathway is strongly inhibited by CP-mediated multimetal starvation in *A. baumannii*, linking the key micronutrient Zn(II) to the central process of protein translation. We focus on a previously uncharacterized Zn(II) metalloenzyme QueD2 as a possible bottleneck in Q-tRNA biosynthesis, given its anticipated role as catalyzing the committed step in the pathway (43). While QueD is considered the housekeeping 6-CPH_4 synthase and QueD2 a "low zinc" paralog (49), *A. baumannii queD2* must fulfill all cellular 6-CPH_4 synthase requirements regardless of the cellular zinc status. While not directly Zur-regulated, *A. baumannii* QueD2 is indistinguishable from Zur-regulated QueD2s at the sequence level and retains "low zinc" features despite serving as the general housekeeping 6-CPH_4 synthase.

The physiological rationale for the high cellular abundance of such "low zinc" paralogs is not broadly understood as recently reviewed (64), but it is typically assumed that a house-keeping enzyme, if present, is unable to access limited Zn(II) in the cell and thus becomes inactivated under conditions of zinc restriction. At least three adaptive scenarios are possible: increased protein abundance, incorporated metal promiscuity, and enhanced Zn(II) acquisition/retention (64). We show here that QueD2 may well exploit all three scenarios, thus illustrating a highly versatile and complex adaptive response to low Zn(II) that can be broadly leveraged by individual organisms as dictated by their environmental niche.

In the simplest case, overexpression alone is used to drive flux through the pathway by mass action (64); i.e., more enzyme competes more effectively for a scarce resource, Zn(II), and in this case, substrate H_2NTP. However, this strategy may be deleterious when that substrate (H_2NTP) defines a true metabolic branch point, here between folate and Q-tRNA biosynthesis in *A. baumannii*. Indeed, Zur-regulated QueD2s are upregulated in low Zn(II), and *A. baumannii* QueD2 becomes cellularly abundant in response to exogenous CP, although not to a level to sustain Q-tRNA biogenesis. Massive, nonphysiological overexpression of QueD2 clearly recovers Q-tRNA flux in a way that is insensitive to CP stress, but this is insufficient in WT *A. baumannii* under normal metabolic control.

Another possibility is that the paralog eliminates or relaxes the strict requirement for the cognate cofactor of the housekeeping enzyme, as observed for the Zur-regulated FolE2 paralog (60, 65) and the Fur-regulated class Ib ribonucleotide reductase, now established as a Mn(II)-cofactored enzyme (3, 66). QueD2 exhibits a ≈100-fold increase in enzymatic turnover in the presence of Fe(II) relative to Zn(II), independent of Cys18, and in striking contrast to *Sa*QueD. Although the origin of this enhancement is unknown, this adaptation may more quickly drive flux through the committed step of the pathway when Zn(II) becomes scarce and Fe(II) remains replete. We note, however, that CP withholds both Zn(II) and Fe(II) from *A. baumannii* in liquid culture (7), and the Fe(II) affinity is unchanged in QueD2 upon introduction of the C18S substitution. Thus, despite the increase in in vitro enzymatic activity, Fe(II) utilization cannot readily explain the resistance to undermetalation observed in the Δ*queD2*::*queD2* strain. However, it is entirely plausible that this property allows QueD2s from this or other organisms to utilize Fe(II) in niches that are specifically starved for Zn(II) but not Fe.

A third adaptive scenario is that the paralog retains specificity for Zn(II) and has evolved some other specific feature(s), e.g., a higher zinc affinity (K_{Zn}) or engagement of a metallochaperone that allows the "low-zinc" paralog to function more effectively under conditions of zinc starvation (67, 68). If the QueD2 K_{Zn1} reports on 50% occupancy in cells (62), this may endow QueD2 with the ability to retain Zn(II) when Zn(II) levels fall even slightly, given a chelatable Zn(II) concentration of ≈10 to 20 pM, for example, that has been measured *in E. coli* without exogenous Zn(II) added to the growth media (69). Analogous measurements have not been made for *A. baumannii*. We note that the affinity of site 2 (K_{Zn2}) is immaterial to this function since this site will only be fully occupied under conditions of cellular Zn(II) toxicity. It is therefore the presence of Cys18 alone that confers this functional advantage, minimizing undermetallation of QueD2 as cellular Zn(II) levels fall. We therefore conclude that Cys18 in metal site 2 is the primary feature that helps to ensure functional QueD2 and Q-tRNA production in *A. baumannii* cells under conditions of CP-induced metal restriction.

The mechanism by which Cys18 enhances the affinity of metal site 1 is unknown. The physical proximity of the metal sites, the distinct active site arrangement, and the highly dynamic nature of the Zn2 loop support a model for rapid metal exchange between QueD2 sites 1 and 2, enhancing the time-averaged occupancy of site 1, ultimately slowing the dissociation of Zn(II) from the active site as metal levels fall. This "metal retention" function of site 2, while modestly compromising the catalytic activity, may well feature an ensemble of active site conformations capable of transiently coordinating the Zn(II) when the substrate is not bound, while also expanding the catalytic metal site promiscuity. An alternative model that is consistent with the Co(II) absorption spectra is the formation of a single high-affinity "hybrid" metal binding site consisting of coordinating residues from Zn1 and the dynamic Zn2 loop, likely Cys18. This site, distinct from the crystallographic Zn1 site, may marginally increase Zn(II) binding affinity, such that QueD2 has enhanced metal occupancy under metal-limiting conditions. This model mirrors studies on the evolution of metallo-β-lactamases, in which small increases in Zn(II) affinity allow antibiotic-resistant pathogens to better adapt to host-imposed nutritional immunity (67). Both models nicely account for a decrease in the Zn(II) dissociation rate mediated by Cys18. In fact, the displaced *tris*-imidazole coordination sphere of Zn1 in our ligand-free QueD2 structure may be reporting on a "plasticity" in the first coordination sphere that enhances metal retention.

The extent to which this degree of complexity underscores the adaptive response in other low-zinc paralogs in other organisms as well as the degree to which a crippling of Q-tRNA biosynthesis

impacts the integrity and composition of the proteome are unknown but remain of considerable interest. Indeed, although tRNA modifications can affect translational regulation (70), recent studies suggest that cotranslational regulation of specific transcripts may also be important (71, 72). The presumed undermetalation of the Q biosynthesis pathway enzymes may represent an evolutionary adaptation to low Zn(II), such that downregulation of Q production results in an increase in translational speed for the few transcripts enriched with NAC codons, which may well be beneficial to growth under conditions of Zn(II) restriction. Further physiological impacts of the loss of Q, in either Zn(II)-replete or Zn(II)-deplete conditions, remain to be evaluated.

Data Sharing Plan

Crystallographic coordinates have been deposited into the protein data bank under PDB ID 7v0f. SSN and genomic neighborhood network (GNN) derived from this work are available as an Excel file and can be found in Supplemental File 1. All other primary data are presented here.

Materials and Methods

A. baumannii cells were grown in a chemically defined HHWm medium at 37 °C, and lysates were prepared in the exponential growth phase. For queuosine quantification, total tRNA was extracted from cells and digested into nucleosides for LC–MS analysis and quantitation. Metal binding experiments were carried out as competition experiments with spectrophotometric dyes mag-fura-2 or quin-2 of known zinc and Fe(II) affinities or via direct titration of the apo-enzyme [Co(II)]. Enzymatic assays were performed by monitoring UV–Vis absorption spectra over time with full spectra subject to kinetic analysis. Detailed *Materials and Methods* can be found in the *SI Appendix*. See *SI Appendix*, Table S1 for data collection and refinement statistics and *SI Appendix*, Table S3 for all oligonucleotides used in this study.

Data, Materials, and Software Availability. Crystallographic data have been deposited in the Protein Data Bank (PDB, 7v0f).

ACKNOWLEDGMENTS. This research is supported by the NIH grants R35 GM118157 (to D.P.G.) and R01 AI101171 (to Eric Skaar, Walter Chazin and D.P.G.). M.R.J. was supported by a graduate training fellowship in Quantitative and Chemical Biology at Indiana University (T32 GM109825, T32 GM131994). We gratefully acknowledge the use of the Macromolecular Crystallography Facility (MCF) and Laboratory for Biological Mass Spectrometry at Indiana University Bloomington. We also thank Jay Nix for his assistance during X-ray data collection at beamline 4.2.2 at Advanced Light Source (ALS) at the Lawrence Berkeley National Laboratory, Berkeley, CA. We thank Dr. Walter Chazin for the gift of calprotectin used in this study and L.E. Hesse and E.P. Skaar for providing the Δ*queD2* mutant *A. baumannii* ATCC 17978 strain.

Author affiliations: [a]Department of Chemistry, Indiana University, Bloomington, IN 47405; [b]Department of Molecular and Cellular Biochemistry, Indiana University, Bloomington, IN 47405; and [c]Laboratory for Biological Mass Spectrometry, Department of Chemistry, Indiana University, Bloomington, IN 47405

1. A. Cvetkovic *et al.*, Microbial metalloproteomes are largely uncharacterized. *Nature* **466**, 779–782 (2010).
2. K. J. Waldron, J. C. Rutherford, D. Ford, N. J. Robinson, Metalloproteins and metal sensing. *Nature* **460**, 823–830 (2009).
3. J. A. Cutrovo Jr., J. Stubbe, Metallation and mismetallation of iron and manganese proteins in vitro and in vivo: The class I ribonucleotide reductases as a case study. *Metallomics* **4**, 1020–1036 (2012).
4. P. G. Sohnle, C. Collins-Lech, J. H. Wiessner, The zinc-reversible antimicrobial activity of neutrophil lysates and abscess fluid supernatants. *J. Infect. Dis.* **164**, 137–142 (1991).
5. J. N. Radin, J. Zhu, E. B. Brazel, C. A. McDevitt, T. E. Kehl-Fie, Synergy between nutritional immunity and independent host defenses contributes to the importance of the MntABC manganese transporter during *Staphylococcus aureus* Infection. *Infect. Immun.* **87**, e00642-18 (2018).
6. A. N. Besold *et al.*, Role of calprotectin in withholding zinc and copper from *Candida albicans*. *Infect. Immun.* **86**, IAI.00779–17 (2018).
7. J. Wang *et al.*, Multi-metal restriction by calprotectin impacts *De Novo* flavin biosynthesis in *Acinetobacter baumannii*. *Cell Chem. Biol.* **26**, 745–755.e7 (2019).
8. T. G. Nakashige *et al.*, The hexahistidine motif of host-defense protein human calprotectin contributes to zinc withholding and its functional versatility. *J. Am. Chem. Soc.* **138**, 12243–12251 (2016).
9. T. G. Nakashige, B. Zhang, C. Krebs, E. M. Nolan, Human calprotectin is an iron-sequestering host-defense protein. *Nat. Chem. Biol.* **11**, 765–771 (2015).
10. E. M. Zygiel, E. M. Nolan, Transition metal sequestration by the host-defense protein calprotectin. *Annu. Rev. Biochem.* **87**, 621–643 (2018).
11. Y. Wang *et al.*, The cellular economy of the *Saccharomyces cerevisiae* zinc proteome. *Metallomics* **10**, 1755–1776 (2018).
12. Y. M. Garcia *et al.*, A superoxide dismutase capable of functioning with iron or manganese promotes the resistance of *staphylococcus aureus* to calprotectin and nutritional immunity. *PLoS Pathog.* **13**, e1006125 (2017).
13. J. N. Radin *et al.*, Metal-independent variants of phosphoglycerate mutase promote resistance to nutritional immunity and retention of glycolysis during infection. *PLOS Pathog.* **15**, e1007971 (2019).
14. B. L. Nairn *et al.*, The response of *acinetobacter baumannii* to zinc starvation. *Cell Host Microbe* **19**, 826–836 (2016).
15. Z. D. Miles, S. A. Roberts, R. M. McCarty, V. Bandarian, biochemical and structural studies of 6-carboxy-5,6,7,8-tetrahydropterin synthase reveal the molecular basis of catalytic promiscuity within the tunnel-fold superfamily. *J. Biol. Chem.* **289**, 23641–23652 (2014).
16. G. Phillips *et al.*, Functional promiscuity of the COG0720 family. *ACS Chem. Biol.* **7**, 197–209 (2012).
17. Y. C. Chen, V. P. Kelly, S. V. Stachura, G. A. Garcia, Characterization of the human tRNA-guanine transglycosylase: Confirmation of the heterodimeric subunit structure. *RNA* **16**, 958–968 (2010).
18. V. de Crécy-Lagard, M. Jaroch, Functions of bacterial tRNA modifications: From ubiquity to diversity. *Trends Microbiol.* **29**, 41–53 (2021).
19. N. Ranjan, M. V. Rodnina, tRNA wobble modifications and protein homeostasis. *Translation* **4**, 1–11 (2016).
20. F. Harada, S. Nishimura, Possible anticodon sequences of tRNAHis, tRNAAsn, and tRNAAsp from *Escherichia coli* B. universal presence of nucleoside Q in the first position of the anticondons of these transfer ribonucleic acids. *Biochemistry* **11**, 301–308 (1972).
21. H. Kasai *et al.*, Structure of the modified nucleoside q isolated from *Escherichia coli* transfer ribonucleic acid. 7-(4,5-cis-dihydroxy-1-cyclopenten-3-ylaminomethyl)-7-deazaguanosine. *Biochemistry* **14**, 4198–4208 (1975).
22. H. J. Grosjean, S. de Henau, D. M. Crothers, On the physical basis for ambiguity in genetic coding interactions. *Proc. Natl. Acad. Sci. U.S.A.* **75**, 610–614 (1978).
23. F. Meier, B. Suter, H. Grosjean, G. Keith, E. Kubli, Queuosine modification of the wobble base in tRNAHis influences "in vivo" decoding properties. *EMBO J.* **4**, 823–827 (1985).
24. F. Tuorto *et al.*, Queuosine-modified tRNAs confer nutritional control of protein translation. *EMBO J.* **37**, 1–14 (2018).
25. M. Müller *et al.*, Queuine links translational control in eukaryotes to a micronutrient from bacteria. *Nucleic Acids Res.* **47**, 3711–3727 (2019).
26. S. Kulkarni *et al.*, Preferential import of queuosine-modified tRNAs into *Trypanosoma brucei* mitochondrion is critical for organellar protein synthesis. *Nucleic Acids Res.* **49**, 8247–8260 (2021).
27. S. Dixit *et al.*, Dynamic queuosine changes in tRNA couple nutrient levels to codon choice in *Trypanosoma brucei*. *Nucleic Acids Res.* **49**, 12986–12999 (2021).
28. N. Manickam, K. Joshi, M. J. Bhatt, P. J. Farabaugh, Effects of tRNA modification on translational accuracy depend on intrinsic codon-anticodon strength. *Nucleic Acids Res.* **44**, 1871–1881 (2015).
29. U. Grädler *et al.*, A new target for shigellosis: Rational design and crystallographic studies of inhibitors of tRNA-guanine transglycosylase. *J. Mol. Biol.* **306**, 455–467 (2001).
30. M. Marchetti *et al.*, Queuosine biosynthesis is required for sinorhizobium meliloti-induced cytoskeletal modifications on hela cells and symbiosis with medicago truncatula. *PLoS One* **8**, e56043 (2013).
31. X. Wang *et al.*, Queuosine modification protects cognate tRNAs against ribonuclease cleavage. *RNA* **24**, 1305–1313 (2018).
32. R. P. Singhal, V. N. Vakharia, The role of queuine in the aminoacylation of mammalian aspartate transfer RNAs. *Nucleic Acids Res.* **11**, 4257–4272 (1983).
33. T. Reisser, W. Langgut, H. Kersten, The nutrient factor queuine protects HeLa cells from hypoxic stress and improves metabolic adaptation to oxygen availability. *Eur. J. Biochem.* **221**, 979–986 (1994).
34. W. Baranowski, G. Dirheimer, J. A. Jakowicki, G. Keith, Deficiency of queuine, a highly modified purine base, in transfer rnas from primary and metastatic ovarian malignant tumors in women. *Cancer Res.* **54**, 4468–4471 (1994).
35. U. Aytaç, U. Gündüz, Q-modification of tRNAs in human brain tumors. *Cancer Biochem. Biophys.* **14**, 93–98 (1994).
36. B. S. Huang, R. T. Wu, K. Y. Chien, Relationship of the queuine content of transfer ribonucleic acids to histopathological grading and survival in human lung cancer. *Cancer Res.* **52**, 4696–4700 (1992).
37. A. Thibessard *et al.*, Identification of Streptococcus thermophilus CNRZ368 genes involved in defense against superoxide stress. *Appl. Environ. Microbiol.* **70**, 2220–2229 (2004).
38. J. M. Durand *et al.*, *vacC*, a virulence-associated chromosomal locus of *Shigella flexneri*, is homologous to *tgt*, a gene encoding tRNA-guanine transglycosylase (Tgt) of *Escherichia coli* K-12. *J. Bacteriol.* **176**, 4627–4634 (1994).
39. S. Noguchi, Y. Nishimura, Y. Hirota, S. Nishimura, Isolation and characterization of an *Escherichia coli* mutant lacking tRNA-guanine transglycosylase. Function and biosynthesis of queuosine in tRNA. *J. Biol. Chem.* **257**, 6544–6550 (1982).
40. L. Pollo-Oliveira *et al.*, The absence of the queuosine tRNA modification leads to pleiotropic phenotypes revealing perturbations of metal and oxidative stress homeostasis in *Escherichia coli* K12. *Metallomics* **14**, mfac065 (2022).
41. P. M. Sharp, W. H. Li, The codon adaptation index–a measure of directional synonymous codon usage bias, and its potential applications. *Nucleic Acids Res.* **15**, 1281–1295 (1987).
42. G. Auerbach *et al.*, Zinc plays a key role in human and bacterial GTP cyclohydrolase I. *Proc. Natl. Acad. Sci. U.S.A.* **97**, 13567–13572 (2000).
43. R. M. McCarty, A. Somogyi, V. Bandarian, *Escherichia coli* QueD Is a 6-carboxy-5,6,7,8-tetrahydropterin synthase. *Biochemistry* **48**, 2301–2303 (2009).
44. M. T. Nelp, V. Bandarian, A single enzyme transforms a carboxylic acid into a nitrile through an amide intermediate. *Angew. Chem. Int. Ed.* **54**, 10627–10629 (2015).

45. S. Chong, A. W. Curnow, T. J. Huston, G. A. Garcia, tRNA-guanine transglycosylase from Escherichia coli is a zinc metalloprotein. Site-directed mutagenesis studies to identify the zinc ligands. *Biochemistry* **34**, 3694–3701 (1995).
46. R. M. McCarty, C. Krebs, V. Bandarian, Spectroscopic, steady-state kinetic, and mechanistic characterization of the radical SAM enzyme QueE, which catalyzes a complex cyclization reaction in the biosynthesis of 7-deazapurines. *Biochemistry* **52**, 188–198 (2013).
47. Z. D. Miles, W. K. Myers, W. M. Kincannon, R. D. Britt, V. Bandarian, Biochemical and spectroscopic studies of epoxyqueuosine reductase: A novel iron–sulfur cluster- and cobalamin-containing protein involved in the biosynthesis of queuosine. *Biochemistry* **54**, 4927–4935 (2015).
48. Q. Li *et al.*, Epoxyqueuosine reductase queh in the biosynthetic pathway to tRNA queuosine is a unique metalloenzyme. *Biochemistry* **60**, 3152–3161 (2021).
49. C. E. Haas *et al.*, A subset of the diverse COG0523 family of putative metal chaperones is linked to zinc homeostasis in all kingdoms of life. *BMC Genomics* **10**, 470 (2009).
50. H. Zeng, X. Zhang, M. Ding, X. Zhang, Y. Zhu, Transcriptome profiles of soybean leaves and roots in response to zinc deficiency. *Physiol. Plant.* **167**, 330–351 (2019).
51. T. J. Siard, K. B. Jacobson, W. R. Farkas, Queuine metabolism and cadmium toxicity in *Drosophila melanogaster*. *Biofactors* **3**, 41–47 (1991).
52. X. Huang, C.-W. Fang, Y.-W. Guo, H.-Q. Huang, Differential protein expression of kidney tissue in the scallop Patinopecten yessoensis under acute cadmium stress. *Ecotoxicol. Environ. Saf.* **74**, 1232–1237 (2011).
53. J. Jo *et al.*, Isolation of ALU1-P gene encoding a protein with aluminum tolerance activity from *Arthrobacter viscosus*. *Biochem. Biophys. Res. Commun.* **239**, 835–839 (1997).
54. A. M. Salzano *et al.*, Redox stress proteins are involved in adaptation response of the hyperthermoacidophilic archaeon *Sulfolobus solfataricus* to nickel challenge. *Microb. Cell Fact.* **6**, 1–11 (2007).
55. B. Águila-Clares *et al.*, Transcriptional response of *Erwinia amylovora* to copper shock: In vivo role of the *copA* gene. *Mol. Plant Pathol.* **19**, 169–179 (2018).
56. J. A. Gerlt *et al.*, Enzyme function initiative-enzyme similarity tool (EFI-EST): A web tool for generating protein sequence similarity networks. *Biochim. Biophys. Acta Proteins Proteomics* **1854**, 1019–1037 (2015).
57. K. A. Edmonds, M. R. Jordan, D. P. Giedroc, COG0523 proteins: A functionally diverse family of transition metal-regulated G3E P-loop GTP hydrolases from bacteria to man. *Metallomics* **13**, mfab046 (2021).
58. A. Mikhaylina, A. Z. Ksibe, D. J. Scanlan, C. A. Blindauer, Bacterial zinc uptake regulator proteins and their regulons. *Biochem. Soc. Trans.* **46**, 983–1001 (2018).
59. N. Colloc'h, A. Poupon, J. P. Mornon, Sequence and structural features of the T-fold, an original tunnelling building unit. *Proteins Struct. Funct. Genet.* **39**, 142–154 (2000).
60. B. Sankaran *et al.*, Zinc-independent folate biosynthesis: Genetic, biochemical, and structural investigations reveal new metal dependence for GTP cyclohydrolase IB. *J. Bacteriol.* **191**, 6936–6949 (2009).
61. H. Nar *et al.*, Active site topology and reaction mechanism of GTP cyclohydrolase I. *Proc. Natl. Acad. Sci. U.S.A.* **92**, 12120–12125 (1995).
62. D. Osman *et al.*, Bacterial sensors define intracellular free energies for correct enzyme metalation. *Nat. Chem. Biol.* **15**, 241–249 (2019).
63. M. L. VanZile, N. J. Cosper, R. A. Scott, D. P. Giedroc, The zinc metalloregulatory protein *Synechococcus* pcc7942 smtb binds a single zinc ion per monomer with high affinity in a tetrahedral coordination geometry. *Biochemistry* **39**, 11818–11829 (2000).
64. M. R. Jordan, M. V. Dujovne, D. A. Capdevila, D. P. Giedroc "Metal ion homeostasis: Metalloenzyme paralogs in the bacterial adaptative response to zinc restriction" in *Reference Module in Chemistry, Molecular Sciences and Chemical Engineering*, (Elsevier, 2022), 10.1016/B978-0-12-823144-9.00161-8.
65. N. Paranagama *et al.*, Mechanism and catalytic strategy of the prokaryotic-specific GTP cyclohydrolase-IB. *Biochem. J.* **474**, 1017–1039 (2017).
66. T. B. Ruskoski, A. K. Boal, The periodic table of ribonucleotide reductases. *J. Biol. Chem.* **297**, 101137 (2021).
67. G. Bahr, L. J. González, A. J. Vila, Metallo-β-lactamases and a tug-of-war for the available zinc at the host–pathogen interface. *Curr. Opin. Chem. Biol.* **66**, 102103 (2022).
68. A. Weiss *et al.*, Zn-regulated GTPase metalloprotein activator 1 modulates vertebrate zinc homeostasis. *Cell* **185**, 2148–2163.e27 (2022).
69. D. Wang, T. K. Hurst, R. B. Thompson, C. A. Fierke, Genetically encoded ratiometric biosensors to measure intracellular exchangeable zinc in *Escherichia coli*. *J. Biomed. Opt.* **16**, 087011 (2011).
70. B. C. Persson, Modification of tRNA as a regulatory device. *Mol. Microbiol.* **8**, 1011–1016 (1993).
71. L. Pollo-Oliveira, V. De Crécy-Lagard, Can protein expression be regulated by modulation of tRNA modification profiles? *Biochemistry* **58**, 355–362 (2019).
72. A. M. Edwards, M. A. Addo, P. C. Dos Santos, Extracurricular functions of tRNA modifications in microorganisms. *Genes (Basel)* **11**, 1–19 (2020).